Original Article

Spatial transcriptomics of gastric cancer brain metastasis reveals atypical vasculature strategies with supportive immune profiles

Kaijing Liu[1,2], Ying Wang[2,3], Chunhua Wang[2,4], Chengcheng Guo[2,5], Dun Zhang[1,2], Yu Zhong[1,2], Lin Yin[6], Yunxin Lu[1,2], Furong Liu[2,7], Yang Zhang[2,7] and Dongsheng Zhang[1,2,8,*]

[1]Department of Medical Oncology, Sun Yat-sen University Cancer Center, Guangzhou, Guangdong, P. R. China
[2]State Key Laboratory of Oncology in South China, Sun Yat-sen University, Guangzhou, Guangdong, P. R. China
[3]Department of Radiation Oncology, Sun Yat-sen University Cancer Center, Guangzhou, Guangdong, P. R. China
[4]Department of Pathology, Sun Yat-sen University Cancer Center, Guangzhou, Guangdong, P. R. China
[5]Department of Neurosurgery/Neuro-oncology, Sun Yat-sen University Cancer Center, Guangzhou, Guangdong, P. R. China
[6]AccuraMed Technology (Guangzhou) Co., Ltd, Guangzhou, Guangdong, P. R. China
[7]Department of Clinical Research, Sun Yat-sen University Cancer Center, Guangzhou, Guangdong, P. R. China
[8]Integrated Traditional Chinese and Western Medicine Research Center, Sun Yat-sen University Cancer Center, Guangzhou, Guangdong, P. R. China

*Corresponding author. Department of Medical Oncology, Sun Yat-sen University Cancer Center, Dongfeng East Road 651, Guangzhou, Guangdong 510060, P. R. China. Tel: +86-20-87343795; Fax: +86-20-87343804; Email: zhangdsh@sysucc.org.cn

Abstract

Background: Gastric cancer brain metastasis (GCBM) represents a rare but highly aggressive malignancy. Metastatic cancer cells are highly heterogeneous and differentially remodels brain vasculature and immune microenvironments, which affects the treatment effectiveness and patient outcome. This study aimed to investigate the spatial interactions among different cell components, especially the vasculature system and the brain microenvironment of GCBM patients.

Methods: We used digital spatial profiling to examine 140 regions composing tumor, immune, and brain tissues from three GCBM patients. Transcriptomic data with spatial information were analyzed for tissue areas related to different blood recruitment strategies. For validation, independent analysis of patient bulk transcriptomic data and *in vivo* single-cell transcriptomic data were performed.

Results: Angiogenesis and blood vessel co-option co-existed within the same GCBM lesion. Tumors with high epithelial-mesenchymal transition and an enhanced transcriptomic gene signature composed of *CTNNB1*, *SPARC*, *VIM*, *SMAD3*, *SMAD4*, *TGFB1*, *TGFB2*, and *TGFB3* were more prone to adopt blood vessel co-option than angiogenesis. Enriched macrophage infiltration, angiogenic chemokines, and *NAMPT* were found in angiogenic areas, while increased T cells, T cell activating cytokines, and reduced *NAMPT* were found in vessel co-option regions. Spatially, angiogenesis was enriched at the tumor edge, which showed higher *DMBT1* expression than the tumor center.

Conclusions: This study mapped the orchestrated spatial characteristics of tumor and immunological compositions that support the conventional and atypical vascularization strategies in GCBM. Our data provided molecular insights for more effective combinations of anti-vascular and immune therapies.

Keywords: gastric cancer brain metastases; spatial transcriptomics; angiogenesis; blood vessel co-option; tumor microenvironment

Introduction

Up to 30%–40% of cancer patients develop brain metastases during tumor progression [1]. Despite the continuous advance in cancer treatment and the overall prolonged survival time, the outcome of brain metastatic patients remains dismal. Brain metastasis typically arises from lung cancer, breast cancer, and melanoma [2, 3]. Gastric cancer brain metastasis (GCBM) represents a rare yet highly aggressive status of cancer progression with an estimated incidence of less than 1% [4–7]. As a result, its tumor microenvironment and transcriptomic characteristics are poorly understood. Although GCBM is rare, the study of such a disease would help to identify unique and shared mechanisms that underline aggressive cancer metastases.

Metastasis is governed by the interactions between malignant cells and host organs under a spatial context, for the biological functions and interactions of cell populations are deeply influenced by their spatial distributions. Spatially resolved transcriptomics is increasingly used to study gene expression patterns with different tissue architectures [8, 9], which has advanced our understanding of tumor microenvironments [10] and helped identify novel therapeutic targets and diagnostic biomarkers [11–15].

Here, we dissected the complex spatial microenvironment of brain metastatic tumors derived from gastric cancer using the Digital Spatial Profiler (DSP) technique. We obtained high-plex spatial transcriptomic data in manually selected regions of

interest (ROI) of GCBM samples. Integrating the spatial transcriptomic and histological data, we found heterogeneous vasculature patterns interacting with distinct tumor and immune characteristics. The co-existence of blood vessel co-option and angiogenesis implies the complexity of tumor vasculature. Hence, a more precise selection of anti-vascular therapies in the clinic is warranted. Moreover, we mapped the metabolic features and cytokine profiles corresponding to different vascular approaches and discovered potentially druggable targets. Our findings highlighted the advantage of spatial transcriptomics as a powerful tool to investigate cancer heterogeneity and tumor microenvironment, which would guide the development of a more specific and effective therapy.

Materials and methods
Patient characteristics and sample collection

This study was approved by the institutional committee of Sun Yat-sen University Cancer Center (SYSUCC), Guangzhou, China. Formalin-fixed and paraffin-embedded (FFPE) samples of brain metastases were obtained from three GCBM patients diagnosed with pathological evidence at SYUCC. Written consent was exemplified by the three patients. The investigation conforms with the principles outlined in the Declaration of Helsinki. Clinical data are available in Supplementary Table S1.

GeoMx human whole transcriptome assay

For the NanoString GeoMx DSP RNA assays, slides were prepared following the manufacturer's User Manual (NanoString, MAN-10115–05 for software v2.3). The Whole Transcriptome Atlas (WTA) probe reagent kit was adopted. The morphology markers, including CD45 (Proteintech, 60287-1-Ig) for leukocytes, PanCK (NanoString, 121300310) for epithelial cells, and DNA stainSYTO13 (NanoString, 121300303) for the nucleus were utilized. Stained slides were loaded onto the NanoString DSP instrument and scanned with a 20× objective. Scan parameters were 50 ms FITC/525 nm, 200 ms Cy3/568 nm, and 200 ms Texas Red/615 nm. Irregular shapes of ROIs for optimal tissue covering were selected based on immunofluorescent signals and histology.

GeoMx RNA Illumina library preparation and sequencing

Oligonucleotide barcodes encoding the target genes were released from their target-specific regions using ultraviolet illumination and then were captured. The library preparation was performed according to the manufacturer's instructions (performed by CapitalBio Technology, Beijing). Illumina adapter sequences and unique dual sample indices were added to the polymerase chain reaction (PCR) amplification process, which allowed PCR products to be pooled together for sequencing. Libraries were sequenced with an Illumina NovaSeq 6000 platform with PE150 mode.

Quality control and data processing

DSP sequencing data were processed with the GeoMx NGS Pipeline. After sequencing, reads were trimmed, merged, and aligned to a list of index oligos to identify the source probe. Each read's unique molecular identifier (UMI) region was used to remove PCR duplicates and duplicate reads. The reads were then converted into digital counts. The limit of quantitation (LOQ) was estimated by the geometric mean with two standard deviations of the negative control probes. Targets that consistently fell below the LOQ were removed from further analysis. The datasets were normalized via upper quartile (Q3) normalization.

Differential gene expression analysis

Differential gene analysis between two groups of ROIs was performed using the Limma R package. A linear model was constructed and modified by empirical Bayes variance moderation to obtain moderated t-statistics. P values were adjusted by multiple false discovery rate (FDR) and a P value of <0.05 was considered statistically significant.

Pathway enrichment analysis

GO enrichment, KEGG enrichment, and Reactome enrichment (human only) of DEGs were performed using EnrichProfiler R-packages with Benjamini–Hochberg multiple testing adjustment. The results were visualized using the R package.

Definition and calculation of scores and signatures

The Z-score of each gene was calculated as follows: the normalized counts of this gene for each ROI were subtracted by the average counts of this gene across all estimated ROIs and then divided by the standard deviation of the gene counts across all ROIs. Epithelial-mesenchymal transition (EMT) score was calculated by mesenchymal signatures (Z-score sum of *AGER*, *FN1*, *MMP2*, *SNAI2*, *VIM*, *ZEB2*) minus epithelial signatures (Z-score sum of *CDH1*, *CDH3*, *CLDN4*, *EPCAM*, *MAL2*, and *ST14*).

Senescence and senescence-associated secretory phenotype (SASP) score

The scores of SASP and senescence of Tumor-ROIs with low and high PanCk expression were analyzed via the gene set variation analysis (GSVA) based on the corresponding DEGs.

Immune cell infiltration analysis

Immune cell infiltration of the spatial transcriptomic data was analyzed using SpatialDecon as previously described [16]. We utilized the "Immune-Gene" module of the TIMER2 web server to investigate the association between NAMPT expression and immune infiltrates (macrophages and CD8+ T cells) of the stomach adenocarcinoma cohort. The TIMER, EPIC, MCPCOUNTER, CIBERSORT, CIBERSORT-ABS, QUANTISEQ, XCELL, and TIDE algorithms were applied. The P values and partial correlation values were computed by the purity-adjusted Spearman's rank correlation test. P values less than 0.05 were considered statistically significant.

Identification and calculation of cancer blood vessel co-opting signatures

Ingenuity pathways analysis (IPA) was conducted based on DEGs between Tumor-ROIs related to angiogenesis and blood vessel co-option. The signature gene list included molecules with top numbers of connections and top predicted upstream regulators. Each signature gene was normalized by subtracting the average gene expression value (all patient samples) from the expression value of each patient sample. The signature score was calculated by summing the normalized expression values for each signature gene.

Single-cell RNA-sequence data analysis

Single-cell RNA-seq raw data were downloaded from ArrayExpresse with accession number E-MTAB-9227. Data met the following criteria were analyzed: contamination rate with mitochondrial genes less than <15%, lower and upper limits of UMI in the range of 300 < genes < 7,000. The R package Seurat was used to cluster the filtered cells. The gene expression matrices were normalized to the total UMI counts per cell and were transformed to the natural log scale. The top 2,000 highly variable

genes (HVGs) from the corrected expression matrix were obtained by the FindVariableFeatures function and then were centered and scaled after cell cycle regression (S and G2M scores were calculated by the CellCycleScoring function in Seurat). Principle component analysis (PCA) on the HVGs was performed, and batch effects were corrected with the RunHarmony function. The FindClusters were used with the clustering parameter resolution 0.5 to identify main cell clusters. Lastly, the RunUMAP function with dimension parameters (1:20) was adopted for visualization.

Results

Spatial transcriptomic atlas of brain metastases from gastric cancer patients

To characterize the spatial microenvironment of brain metastasis in GCBM patients, we identified three patients diagnosed with GCBM with pathological evidence from SYSUCC patient database. The FFPE tissues with satisfactory RNA qualities were collected and applied to the NanoString GeoMx DSP platform (Figure 1A).

To perform the DSP transcriptomic analysis, tissue sections were co-stained with SYTO13 and fluorescently labeled antibodies targeting PanCK and CD45, which specifically label the nucleus, epithelial cells, and immune cells, respectively (Figure 1A). Hematoxylin and eosin (HE) staining were used for morphology examination. The clinical and histological characteristics of the patients are summarized in Supplementary Table S1. ROIs were selected based on immunofluorescence signals and morphology to improve precision. The ROIs were classified into Tumor-ROIs (regions with positive PanCK staining and tumor morphology), Immune-ROIs (regions with positive CD45 staining and immune cell histology), and Brain-ROIs (based on histological features). For each tissue slide, we selected 47 ROIs with one additional ROI as control. Finally, RNA from 140 ROIs was collected for sequencing and downstream analysis (Data from three control ROIs and one ROI from Patient 3 with low RNA quality were not used for final analysis)(Figure 1A). The distribution of ROIs for each metastatic lesion was summarized in Figure 1B. The unequal numbers of ROIs for each patient were due to their morphological differences (Figure 1B). More Immune-ROIs were selected from Patient 1 and Patient 2 due to higher heterogeneity of the immune components in the tumor microenvironment. Due to the lower cellular density, the Immune-ROIs and Brain-ROIs have larger areas but smaller cell counts than the Tumor-ROIs (Figure 1C and D).

Then, the DSP WTA experiment was conducted [17] with RNA transcript quantitated by Illumina sequencing. Qualified
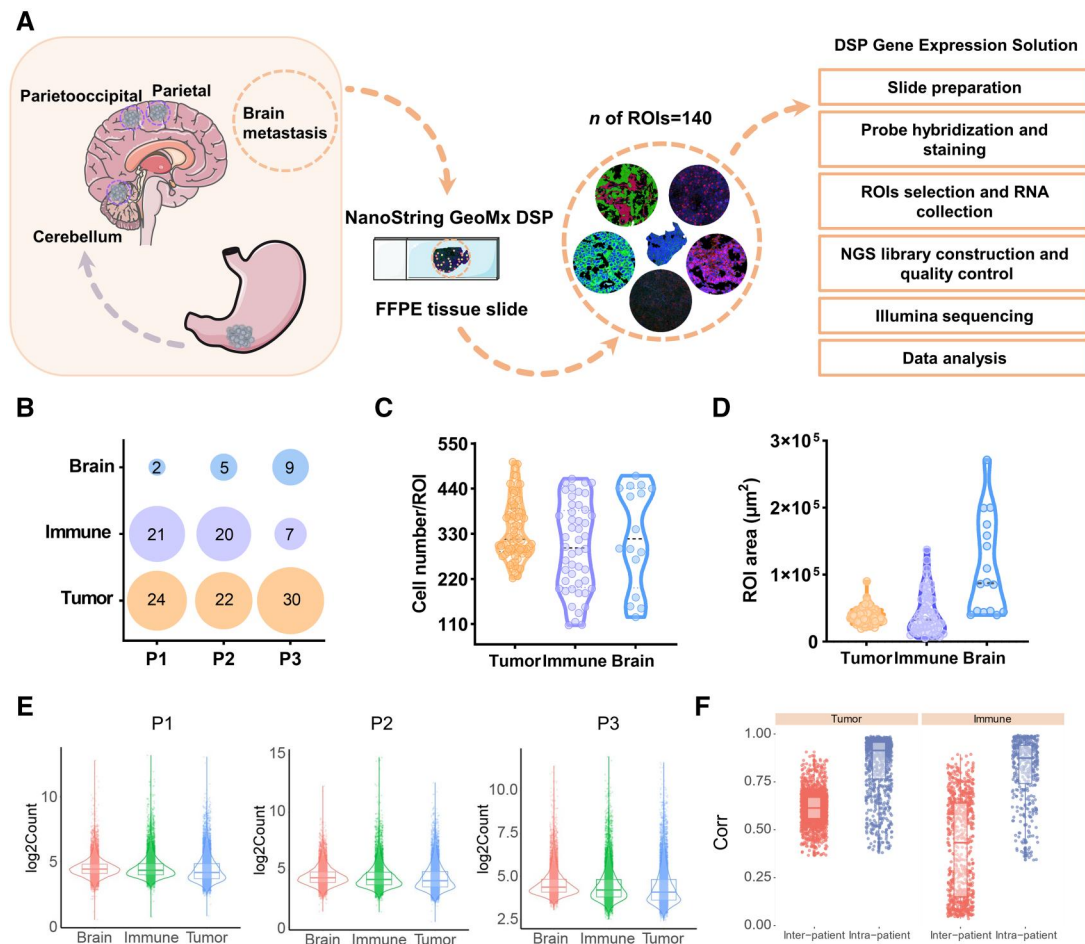

Figure 1. Spatial transcriptomic profiling of intracranial metastases from gastric cancer. (A) Schematic illustration of DSP experimental design. (B) Distribution of ROI types from each patient. ROI types were divided into Tumor-ROI, Immune-ROI, and Brain-ROI based on major compositions inside. Distribution of cell count per ROI (C) and ROI area (D) by ROI type. (E) Violin plots of RNA count per ROI by type and patient. (F) Boxplot showing the interpatient and intrapatient correlation across tumor- ($n = 76$) and immune- ($n = 48$) ROIs. Figure 1A was modified using the Servier Medical Art (http://smart.servier.com). DSP = digital spatial profiler; ROI = region of interest.

sequencing data (mapping rate > 50%, saturation > 50%) were applied to further analysis. One ROI of Patient 3 was excluded from further analysis due to a low mapping rate. The gene count distribution of ROIs per patient is illustrated in Figure 1E. Transcript measurement analysis revealed higher heterogeneity of Immune-ROIs than Tumor-ROIs. The two ROI types both showed higher interpatient than intrapatient heterogeneity (Figure 1F).

Heterogeneous epithelial-mesenchymal transition, proliferation, and senescence of tumor cells

When selecting ROIs, we noticed tumor components exhibited varied PanCK expressions (Figure 2A), consistent with the previously reported epithelial heterogeneity of tumor cells [18]. As EMT is a frequently observed biological switch of cancer cells, we postulated that Tumor-ROIs may have different EMT statuses. We hence estimated the EMT scores of all the Tumor-ROIs. As expected, all patients showed uneven EMT scores, indicating varied EMT status within a single tumor (Figure 2B). In addition,

Tumor-ROIs with low PanCK expressions showed higher EMT scores than those with high PanCK expressions (Figure 2C).

To further explore the molecular properties of Tumor-ROIs with low and high PanCK expression (noted as LowCK and HighCK), we analyzed the differentially regulated genes (DEGs) between LowCK and HighCK Tumor-ROIs in each patient (Figure 2D, E, and F for Patient 1, 2, and 3, respectively). For LowCK Tumor-ROIs of Patient 1, *TWIST1*, a typical mesenchymal signature gene, was significantly upregulated (Figure 2D), consistent with its high EMT status. Genes associated with matrix remodeling, including *FBN2, LUM, COL9A3, COL26A1, COL1A2,* and *SPARC*, were significantly upregulated in LowCK Tumor-ROIs, indicating an active interaction of tumor cells with the surrounding extracellular matrix (ECM) (Figure 2D). For Patient 2, consistent with the loss of PanCK, *EPCAM* was significantly downregulated (Figure 2E). In Patient 2 and Patient 3, the LowCK Tumor-ROIs exhibited high proliferation markers *MZT2B* and *STMN1*, respectively (Figure 2E and F). We then checked the *STMN1* transcript counts of Patient 1 and observed a higher *STMN1* expression in LowCK Tumor-ROIs than in HighCK areas (Supplementary Figure S1A). Pathway enrichment analysis
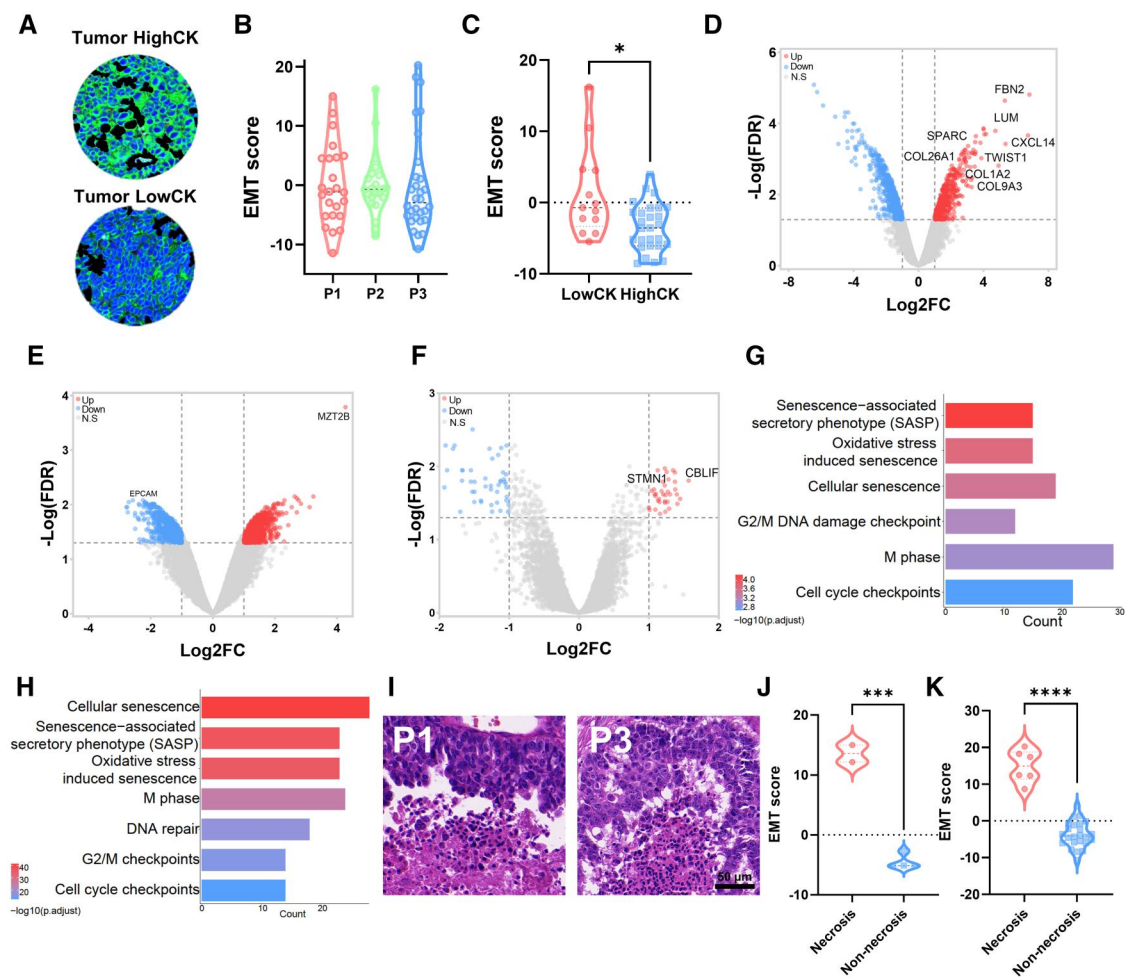

Figure 2. Heterogeneity of cancer cell EMT, proliferation, and senescence revealed by DSP transcriptomics. (A) Representative immunofluorescent staining indicating heterogeneous PanCK expression in Tumor-ROIs: HighCK (up) and LowCK (down). (B) Violin plots of EMT scores based on RNA count across all tumor ROIs by the patient. (**C**) Comparison of EMT scores between Tumor-ROIs with low and high PanCK expression. *$P = 0.0235$ calculated by Welch's *t*-test. Volcano plots showing differentially expressed genes (DEGs) between Tumor-ROIs with low and high PanCK expression in Patient 1 (D), Patient 2 (E), and Patient 3 (F). Pathway enrichment analysis of upregulated DEGs between Tumor-ROIs of low and high PanCK expression from Patient 1 (G) and Patient 3 (H). (I) Representative HE staining indicated necrotic areas in Patient 1 (left) and Patient 3 (Right). Scale bar: 50 μm. Comparison of EMT scores between Tumor-ROIs with and without necrosis in Patient 1 (J) and Patient 3 (K). ***$P = 0.0001$, **** $P < 0.0001$. Statistical test: unpaired *t*-test. CK = cytokeratin; EMT = epithelial-mesenchymal transition; DEGs = differentially expressed genes.

further confirmed the high proliferative status in tumor areas with low PanCK expressions. However, a senescent state with elevated SASP was observed for Patient 1 and Patient 3 (both showed intestinal Lauren type) (Figure 2G and H). Furthermore, necrosis was observed in the intestinal type (Patient 1 and Patient 3) but not the diffuse type (Patient 2) metastases, indicating differences between the two Lauren types (Figure 2I). The necrotic tumor foci also showed higher EMT scores than other tumor parts within the same patient (Figure 2J and K).

In summary, heterogeneous EMT status was observed in all patients. Tumor cells with lower PanCK expression exhibited higher proliferative properties despite cellular senescence and higher levels of SASP. Parts of LowCK tumor areas showed an increased interaction with the ECM.

Different blood vessel recruitment strategies co-exist in individual tumors with orchestrated immune responses

We next investigated the vasculature systems and observed the presence of angiogenesis in all patients examined in this study (Figure 3A). In Patient 1, co-existence of angiogenesis and blood vessel co-option, a non-angiogenic process where tumors hijack pre-existing blood vessels, was observed (Figure 3A).

For both blood vessel recruitment strategies, considerable immune cell infiltration was observed (Supplementary Figure S1B). To investigate the immune programs associated with vascularization, we conducted the Danaher & Kim method-based SpatialDecon to deconvolute mixed types of immune cells using the spatially resolved gene expression datasets [16]. The proportion of each cell type based on calculated abundance is shown in heatmaps (Figure 3B). The quantification analysis revealed a significantly increased abundance of CD8$^+$ memory T cells, CD4$^+$ memory T cells, and plasma cells, meanwhile a decreased abundance of macrophages, in the blood vessel co-option areas compared with those in the angiogenic regions (Figure 3C–F). Although there was no statistically significant difference regarding the fibroblasts, an increasing tendency in the vessel co-option area was observed (Figure 3G).

To further investigate the molecular signatures of the immune cells, we obtained the DEGs between Immune-ROIs related to vessel co-option (Imm-VCO) and those to angiogenesis (Imm-ANG). Both nearby (close to angiogenic areas) (Figure 3H and I) and remote (far from angiogenic areas) Imm-ANG (Figure 3J and K) were compared to Imm-VCO. Volcano plots of DEGs showed an upregulation of immunoglobulin heavy chain genes like IGKC, IGHG1, IGHG2, IGHG3, and IGHG4 in Imm-VCO, suggesting an activated status of plasma cells (Figure 3H and J), which was consistent with that of the elevated plasma cells indicated by immune infiltration analysis. IL32 was also upregulated in Imm-VCO, which is essential for the induction and activation of T cells. Furthermore, the upregulation of IL7R, TRAC, CD8A, CD3D, CD2, LTB, and SELL in Imm-VCO supported the increased T-cell infiltration in those areas. Consistently, XCR1, which is critical for the antigen cross-presentation of dendritic cells to activate CD8+ T cells [19], was also upregulated in Imm-VCO, further implying a higher T cell, especially CD8+ T cell infiltration (Figure 3H and J). However, the enhanced transcript count of immune checkpoint gene IDO1 in Imm-VCO indicated a relatively exhausted T cell state. Pathway enrichment analysis illustrated more activated B and T cell functions of Imm-VCO, indicating a potential benefit of immunotherapy in tumors adopting vessel co-option (Figure 3I and K). Meanwhile, genes related to cell-matrix interaction, such as COL3A1, COL1A2, COL6A1, COL6A2, and fibroblast-specific genes (LUM and DCN), were highly upregulated

in Imm-VCO, indicating a higher infiltration of fibroblasts and more active ECM interaction.

On the contrary, genes associated with M2 macrophages (MSR1, CD163) were significantly upregulated in Imm-ANG (Figure 3H), consistent with the reported pro-angiogenic and immune-inhibitory function of M2 macrophages. Moreover, we observed SPP1, a marker for tumor-associated macrophages (TAM), was significantly increased in nearby and remote Imm-ANG compared with those in Imm-VCO (Figure 3H and J), which was in line with their previously reported strong angiogenic signature [20, 21]. Besides, CXCL9, a chemokine reported to inhibit angiogenesis [22], showed a reduced expression in Imm-ANG, suggesting a different cytokine profile between vessel co-option and angiogenesis.

Immuno-cellular niches with different vasculatures feature diverse immune checkpoint profiles and nicotinamide phosphoribosyltransferase expression

When comparing with Imm-ANG, Imm-VCO showed a significant decreased expression of nicotinamide phosphoribosyltransferase (NAMPT) (Figure 3H and J). NAMPT is a critical enzyme in nicotinamide adenine dinucleotide (NAD+) metabolism and has been reported to modulate immune microenvironment, PD-L1 expression, and hence the efficacy of immunotherapy [23, 24]. We then investigated if NAMPT expression affects immune cell infiltration and expression of immune checkpoints. Results revealed that NAMPT expression positively correlated with the expression of macrophage marker CD68 but negatively with CD8$^+$ T cell marker CD8A (Figure 4A). This finding was verified by analyzing the data of stomach adenocarcinoma (STAD) patients from the TCGA database via TIMER 2.0 (Figure 4B), indicating the potential immune-modulating roles of NAMPT.

NAMPT also correlates with the functional states of immune cells [23]. The Imm-VCO showed an increased expression of checkpoint molecule IDO1 but decreased NAMPT, implying a relatively exhausted state of infiltrated T cells (Figure 3H and J). This observation prompted further analysis to investigate if NAMPT influences other checkpoint molecules. We found that, like with IDO1, NAMPT correlated negatively with the expression of most checkpoint protein genes, including PDCD1, LAG3, CD274, TIGIT, CTLA4, and VSIR, but positively with CD276 and HAVCR2 (respective r and P values are shown in Figure 4C).

To see if the two vascular systems influence the immune cell functions, we next investigated other immune checkpoint proteins of Imm-VCO and Imm-ANG. A comparison of normalized DSP transcript count revealed that PDCD1, CTLA4, TIGIT, and IDO1 were relatively higher in Imm-VCO than in Imm-ANG (Figure 4D, E, and F). On the contrary, HAVCR2 showed higher expression in the Imm-ANG than in Imm-VCO (Figure 4G). Besides, other immune checkpoint proteins like CD274, LAG3, VSIR, and CD276 exhibited similar expression levels in both types of Immune-ROIs (Supplementary Figure S2).

To further investigate if the immune cells show different response patterns according to different blood vessel types, we compared Immune-ROIs close to the artery and vein within the brain tissues with Immune-ROIs within the tumor mass (Figure 5A). The SpatialDecon calculation showed that Immune-ROIs near the brain artery primarily harbored macrophages, but those near the vein, mainly B and T cells (Figure 5B, Supplementary Figure S3). Moreover, Immune-ROIs close to the artery highly recapitulated angiogenesis-related Immune-ROIs in terms of NAMPT, PDCD1, CTLA4, TIGIT, and HAVCR2 expression (Figure 5C–G), showing that angiogenesis created an immune
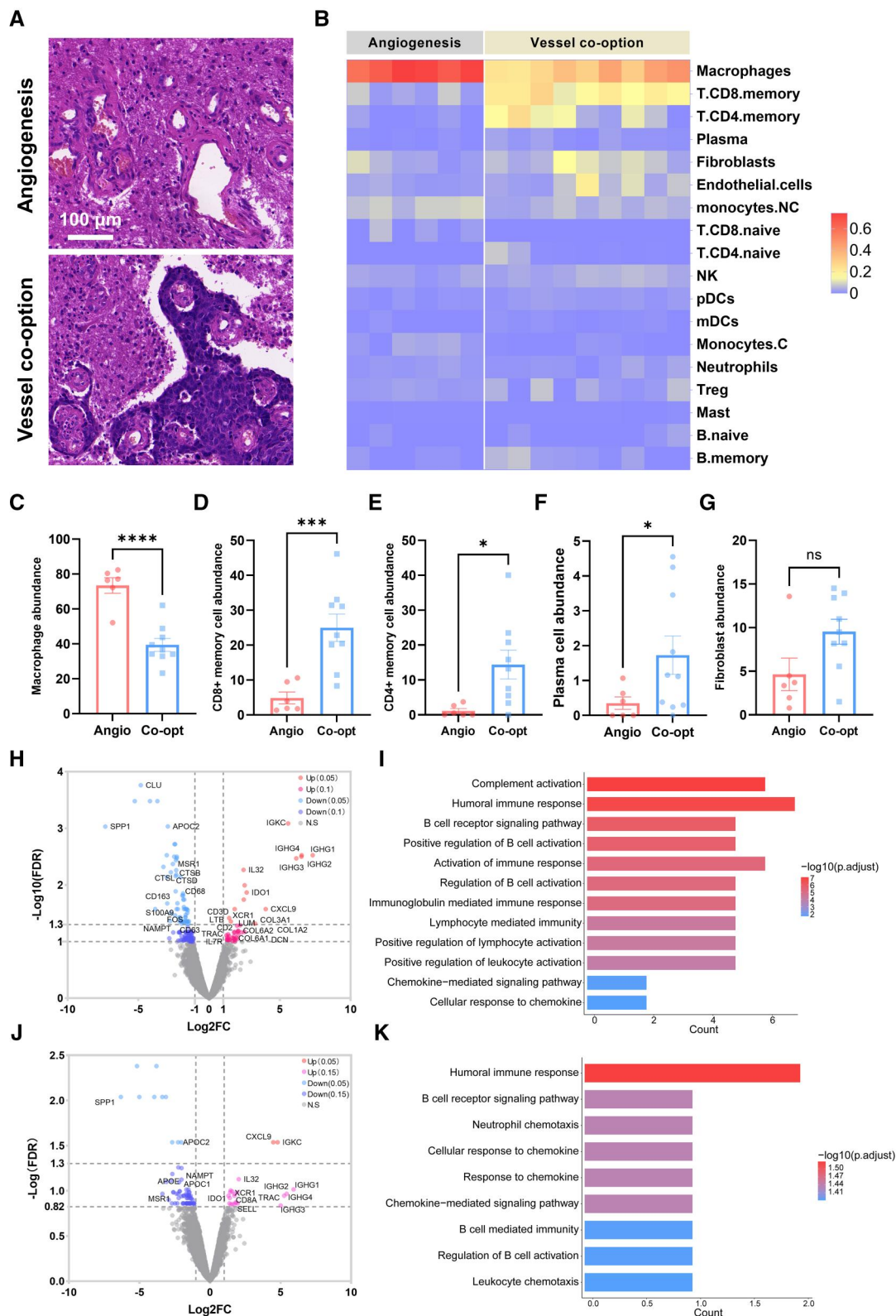
Figure 3. Varied blood vessel recruitment strategies with distinct immune responses co-exist in one tumor lesion. (A) Representative HE staining of angiogenesis (up) and blood vessel co-option (down) from Patient 1. Scale bar: 100 μm. (B) Heatmap illustrating immune cell infiltration in angiogenesis and vessel co-option areas based on calculated cell proportion per ROI via SptatialDecon. Quantitative comparison of SpatialDecon-calculated cell count per ROI between angiogenesis and vessel co-option related Immune-ROIs for macrophage (C), CD8+ memory T cell (D), CD4+ memory T cell (E), plasma cell (F), and fibroblast (G). *P < 0.05, ***P < 0.001, ****P < 0.0001. Statistical test: unpaired t-test or Welch's t-test based on F-test. Volcano plots demonstrating DEGs between Immune-ROIs of vessel co-option and nearby angiogenesis areas (H) and the upregulated pathways of vessel co-option-related Immune-ROIs based on Gene Ontology database (I). Volcano plots demonstrating DEGs between Immune-ROIs of vessel co-option and remote angiogenesis areas (J) and the upregulated pathways of vessel co-option-related Immune-ROIs based on the Gene Ontology database (K). DEGs = differentially expressed genes; ROI = region of interest.
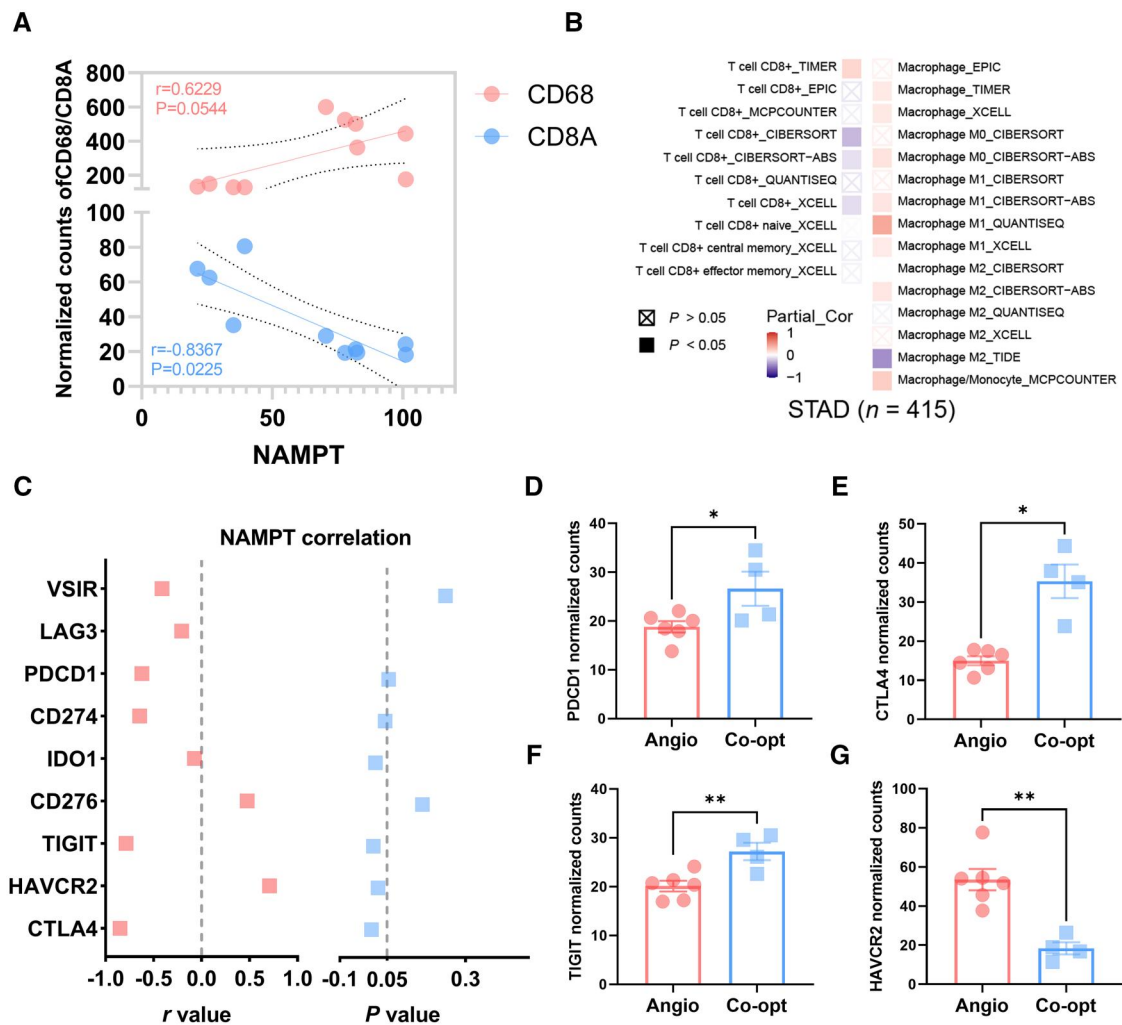
Figure 4. Distinct immune checkpoint profiles associated with *NAMPT* and vascular strategies (A) Correlation between *NAMPT* transcripts and macrophage (CD68) and CD8+ T (CD8A) cell markers in Immune-ROIs associated with different vascular strategies. Statistical analysis: Pearson correlation. (B) Correlation between *NAMPT* expression and CD8+ T cells and macrophages from stomach adenocarcinoma patients via TIMER 2.0 database. (C) Correlation analysis of *NAMPT* levels with different checkpoint molecules expression in Immune-ROIs. Statistical analysis: Pearson correlation. Comparison of various immune checkpoint markers *PDCD1* (D), *CTLA4* (E), *TIGIT* (F), and *HAVCR2* (G) between Immune-ROIs associated with angiogenesis and blood vessel co-option. *P < 0.05, **P < 0.01. Statistical tests: unpaired *t*-test or Welch's *t*-test depends on the *F*-test. Error bars represent ± SEM.

microenvironment more similar to areas around the artery, while blood vessel co-option more similar to that of the vein.

Overall, different blood recruitment strategies led to varied immune cellular paradigms and distinct checkpoint profiles. The strong correlation between *NAMPT* and the observed shift of the immune cell types indicated that *NAMPT* might regulate the interplay between the vascular and immune systems.

Spatial transcriptomic characteristics of brain parenchyma harboring angiogenic blood vessels

To investigate the differences between brain tissues harboring angiogenic blood vessels and those containing established brain blood vessels (Supplementary Figure S4), we compared the immune cell infiltration between Brain-ROIs with and without angiogenesis based on SpatialDecon (Figure 6A). Statistical analysis of the immune cell type supported a higher proportion of endothelial cell and fibroblast, while a lower CD8+ naïve cell proportion in brain areas with angiogenesis (Supplementary Figure S5). Correspondingly, enhanced fibroblast-related genes and ECM remodeling-associated genes were also observed in the brain parenchyma with angiogenesis (Figure 6B and C).

As the angiogenic vessels were prominently enriched at the edge of the tumor in Patient 3, we then compared the Tumor-ROIs located at the edge and core regions of the cancer to see how angiogenesis interacted with cancer cells. We found that expression of Deleted in Malignant Brain Tumors 1 (*DMBT1*) was upregulated in Tumor-ROIs from the tumor edge (Figure 6D) regardless of the PanCK expression (Figure 6E). DMBT1 was reported to be upregulated under hypoxia and has a binding site for *HIF1A*, which is critical for angiogenesis under hypoxic conditions [25]. Correlation analysis revealed that transcript counts of *DMBT1* were positively correlated with *HIF1A* ($r = 0.47$, $P = 0.06$), indicating a potential role of *DMBT1* in stimulating angiogenesis (Figure 6F).

Distinct cancer characteristics associated with blood vessel recruitment strategies

We then explored cancer properties related to different vasculature systems. By comparing angiogenesis-related and vessel co-option-related Tumor-ROIs (short as Tumor-VCO and Tumor-ANG), we found that the Tumor-VCO exhibited a higher *ZEB2* transcript count and EMT score, indicating a stronger adhesive
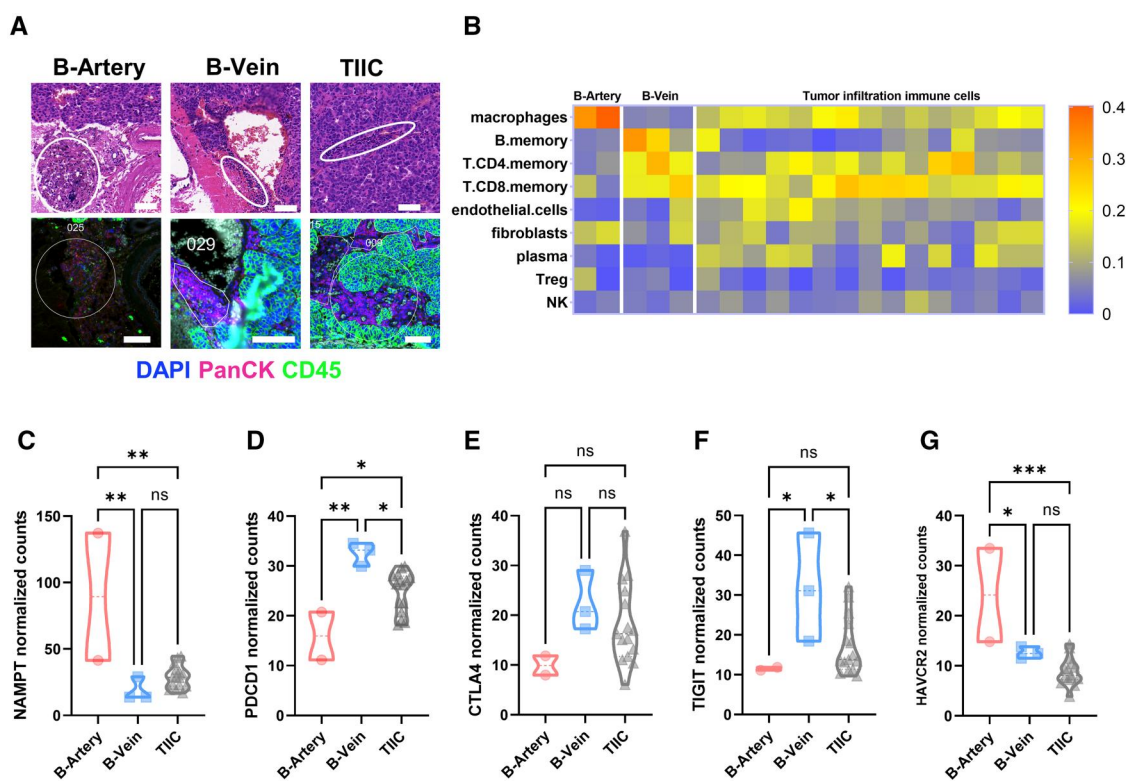
Figure 5. NAMPT and immune checkpoint profiles in immune repertoires near brain artery and vein. (A) Representative HE (upper) and IF (lower) pictures of different Immune-ROIs containing leukocytes that are close to brain artery, brain vein, and within the tumor mass. Scale bar: 100 μm. (B) Heatmap illustrating varied SpatialDecon calculated immune cell type proportion in Immune-ROIs close to a brain artery, brain vein, and within tumor mass. Transcript counts of *NAMPT* (C), *PDCD1* (D), *CTLA4* (E), *TIGIT* (F), *HAVCR2* (G) in Immune-ROIs close to a brain artery, brain vein, and within tumor mass. *$P < 0.05$, **$P < 0.01$. Statistical tests: one-way ANOVA. B-Artery = brain artery; B-Vein = brain vein; TIIC = tumor infiltration immune cells; ROI = region of interest.

and mobile capacity of the cancer cells (Figure 7A and B). This is consistent with the results of previous studies showing that tumors prone to adopt vessel co-option have enhanced EMT and adhesive ability [26]. Further analysis of DEGs between Tumor-VCO and Tumor-ANG revealed a more heterogeneous tumor feature (Figure 7C). Pathways critical for regulating cell mobility, including EMT transition and focal adhesion, were upregulated in Tumor-VCO, further supporting the enhanced mobility of the cancer cells adopting vessel co-option over angiogenesis (Figure 7D). Meanwhile, Tumor-VCO showed reduced expressions of *VEGFA*, *LCN2*, and *SOX9*, which are all reported to support angiogenesis (Figure 7C) [27, 28]. Accordingly, pathway enrichment revealed significantly downregulated angiogenesis-related pathways, such as the response to decreased oxygen levels or hypoxia, the regulation of angiogenesis, and vasculature development in Tumor-VCO, further supporting much-reduced angiogenic activity in blood vessel co-option-related tissues (Figure 7E). Furthermore, angiogenic chemokines like *CXCL5* were upregulated in Tumor-ANG. At the same time, *CXCL9* and *CXCL14*, proposed as angiogenesis inhibitors, were increased in Tumor-VCO (Figure 7C), suggesting a distinct chemokine program related to tumor vascularization strategies. We next did IPA analysis based on the DEGs between Tumor-VCO and Tumor-ANG (Figure 7F) and proposed a signature (*CTNNB1*, *SPARC*, *VIM*, *SMAD3*, *SMAD4*, *TGFB1*, *TGFB2*, and *TGFB3*) for distinguishing tumors associated with blood vessel co-option, denoted as Vco score. The Vco score was established based on selected genes with top number of connections and top upstream predicted regulators from IPA analysis (Figure 7G) [29]. To validate the robustness of the Vco score, we searched the public

databases and found the only two available datasets with provided information with tumor vascularization information: GSE151165 [30] (patient transcriptomic data) from the GEO database and E-MTAB-9227 [37] (mice single-cell RNA-seq data) from the ArrayExpress database. For GSE151165, the Vco score was significantly higher in tumor samples with blood vessel co-option than with angiogenesis (Figure 7H). For E-MTAB-9227 single-cell RNA-seq data, we first clustered cell groups and identified cancer cells (Cluster 0, 5, and 6) based on the specific tumor markers (Figure 7I and Supplementary Figure S6). In this cohort, blood vessel was induced by the angiogenesis inhibitor sunitinib. We then calculated the Vco scores for all groups and found that the sunitinib-treated group exhibited significantly enhanced Vco scores. Both findings confirmed the validity of the Vco score established in this study (Figure 7J). Taken together, tumors with high mobility and EMT status were more likely to adopt vessel co-option than angiogenesis, and varied cytokine profiles were orchestrated to support the corresponding vasculature approaches.

Discussion

GCBM is rare in clinics, representing a highly aggressive case of cancer metastasis. The molecular features underlining GCBM may represent shared biological mechanisms of severe malignancies that drive the metastatic behavior of cancer cells regardless of the primary site. How cancer cells interact with the brain microenvironment is poorly understood. Here, we provided a comprehensive spatial transcriptomic atlas of GCBM.
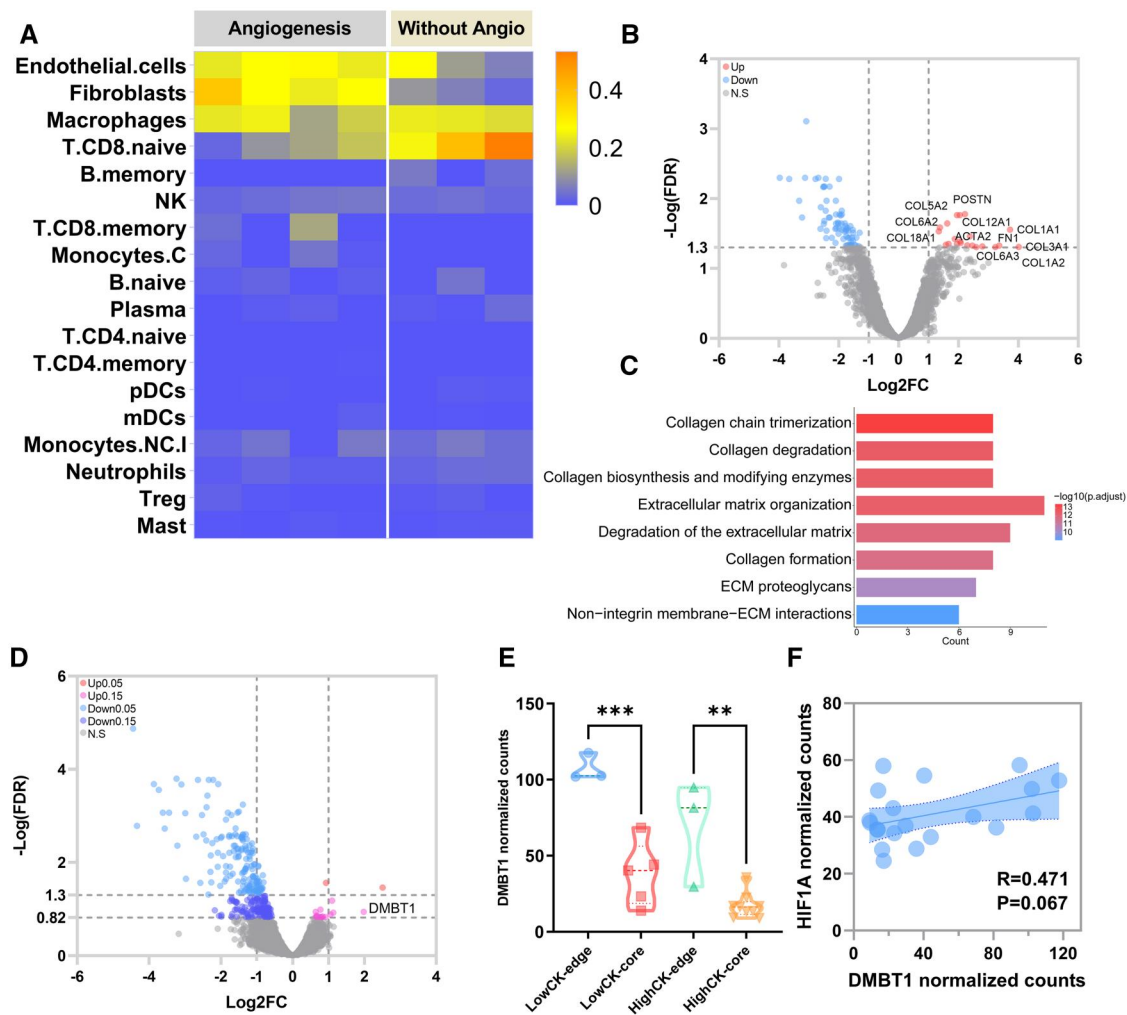
Figure 6. Characteristics of immune cellular niche in brain tissues with and without angiogenesis and identification of potential angiogenic player. (A) Heatmap showing immune cell proportion per ROI of Brain-ROIs with and without angiogenesis based on SpatialDecon calculation. (B) Volcano plot illustrating the DEGs between Brain-ROIs with and without angiogenesis. (C) Pathway enrichment analysis demonstrating upregulated pathways in Brain-ROIs with angiogenesis compared to that without. (D) Volcano plot indicating *DMBT1* upregulation in edge compared to core regions of tumor mass. (E) Statistical analysis of *DMBT1* transcript count between Tumor-ROIs on edge and core regions of tumor according to different PanCK status. **$P < 0.01$, ***$P < 0.001$. Statistical test: one-way ANOVA. (F) Correlation analysis between *DMBT1* and *HIF1A* transcript count of Brain-ROIs on edge and core of tumor mass. ROI = region of interest.

We identified the co-existence of blood vessel co-option and angiogenesis within the same GCBM tumor focus. Vascular system remodeling is critical for cancer metastasis and colonization. Angiogenesis has long been regarded as the most important tumor blood supply approach. However, vessel co-option, a non-angiogenic process where cancer cells hijack pre-existing blood vessels for blood and nutrition supply, has recently gained increased attention [26, 31]. Tumor cells can favor blood vessel co-option rather than angiogenesis when metastasizing to highly vascularized organs, such as the liver and brain [31, 32]. As tumors adopting blood vessel co-option are intrinsically poor responders to this treatment [32–34], the finding of co-existence of blood vessel co-option and angiogenesis could explain the less satisfactory anti-VEGF therapy outcome in the clinics. This further suggests that a more precise patient selection for anti-VEGF therapies is warranted since blood vessel co-option implies pre-existing resistance and potential rapid disease progression [26, 32, 33]. Furthermore, molecular pathways involved in vessel co-option are poorly understood, and the identification of blood vessel co-option mainly relies on histological examinations. Histomorphology-based Lauren subtyping has been generally used in clinics to categorize gastric cancers, but the identification of vessel co-option is far less established. Our finding highlights the importance of pathological examination of vascular morphology, which could support clinicians in making better anti-vascular treatment decisions in clinical practice.

The tumor microenvironment is a highly complex cellular niche where vascular systems and immune components influence each other. Recently, the combination of anti-vascular and immune checkpoint inhibitors has been reported to improve outcomes of selected cancer patients [35–37]. Hence, we found that increased T cells were observed in blood vessel co-option-related areas, while macrophage (especially M2 and SPP1+ TAM) infiltration was more prominent in angiogenic areas. The high infiltration of T cells indicated a potential response toward immunotherapy for GCBM patients with blood vessel co-option. Macrophages are critical players in the metastatic ecosystem with a well-described M1/M2 polarization paradigm. SPP1+ TAMs exhibited higher M2 signatures with an angiogenic gene expression program [38] and thus have been regarded as pro-angiogenic [21]. Our observation of higher M2 and SPP1+ TAMs in angiogenesis-related areas supported their previously reported
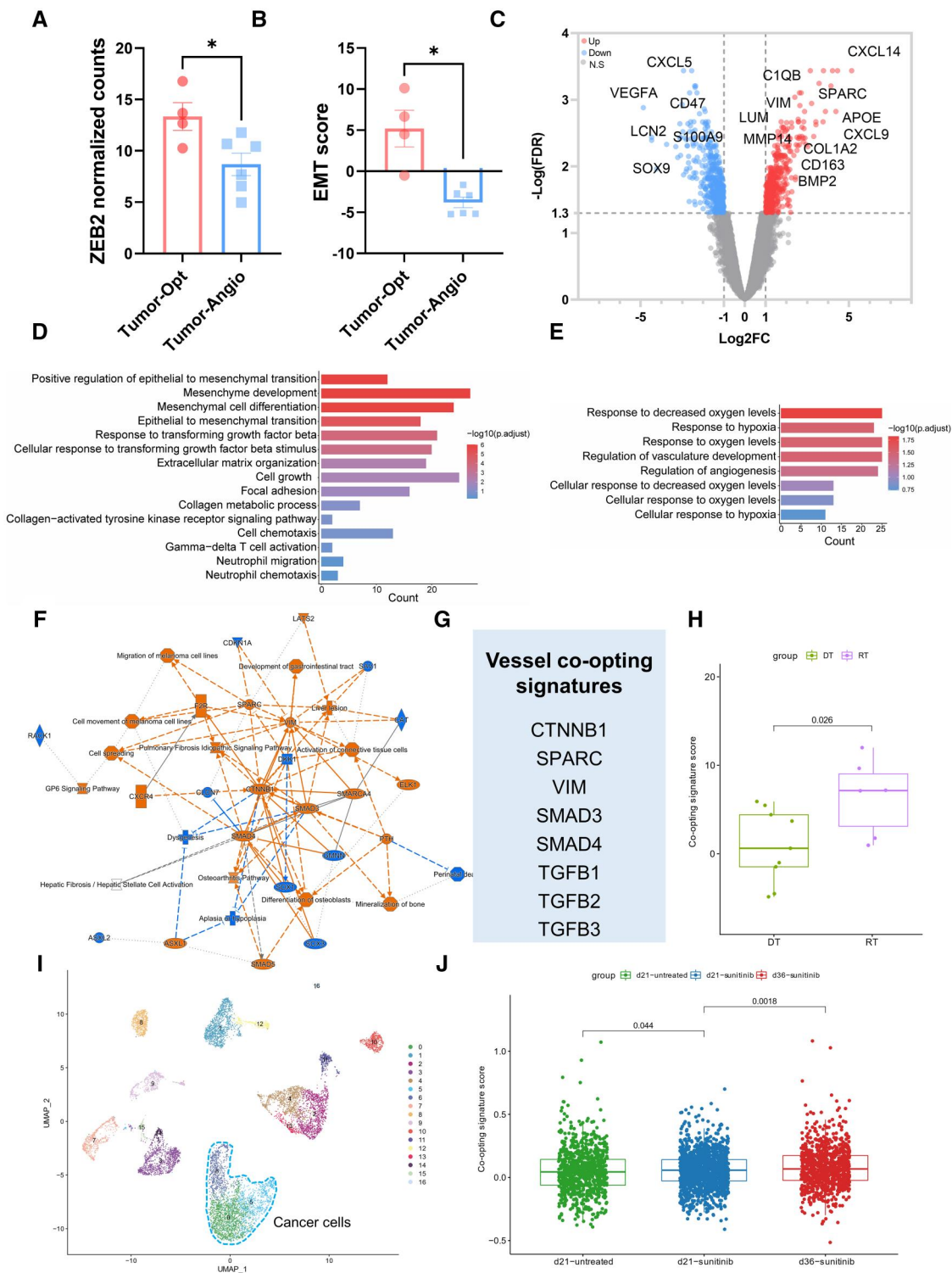
Figure 7. Characteristics of cancer cell adopting different vascular recruitment strategies. Quantification of tumor cell mobility related gene-ZEB2 (A) and EMT signature (B) in Tumor-ROIs related with angiogenesis and vessel co-option areas. Statistical tests: unpaired *t*-test or Welch's *t*-test depending on F-test. Error bars represent SEM. (C) Volcano plot illustrating DEGs between Tumor-ROIs derived from angiogenesis and blood vessel co-option-related areas. Upregulated (D) and downregulated (E) signaling pathways in Tumor-ROIs with vessel co-option compared to those with angiogenesis by pathway enrichment analysis based on Gene Ontology or KEGG database. (F) Graphical summary of major molecules and connections based on IPA analysis. (**G**) Inferred blood vessel co-option signature gene list of cancer cells based on IPA analysis. (**H**) Validation of cancer Vco score for differentiating tumors with various vasculatures based on GEO (GSE151165). DT and RT respectively adopted angiogenesis and blood vessel co-option as their main blood supply strategy. (**I**) UMAP figure illustrating cell clusters of single-cell RNA-seq data of ArrayExpress (E-MTAB-9227) which contains cancer cells adopting blood vessel co-option and angiogenesis. (**J**) Vco score increases with the increment of vessel co-opting cancer cell proportion in samples. SEM = standard error of the mean; DEGs = differentially expressed genes; KEGG = Kyoto Encyclopedia of Genes and Genomes; IPA = ingenuity pathway analysis; DT = tumors with desmoplastic growth pattern; RT = tumors with replacement growth patterns; GEO = gene expression omnibus; UMAP = uniform manifold approximation and projection.

angiogenic functions [21]. We also summarized the immune checkpoint profiles associated with angiogenesis and blood vessel co-option. Angiogenesis and blood vessel co-option remodel the immune microenvironment, resembling that of the artery and vein, respectively. This indicates a fundamental difference between the two vascular systems. Overall, these results indicated the necessity for a more precise and flexible design when combining immune checkpoint inhibitors with anti-vascular therapies.

Cancer cells are highly adaptable under selective pressures from the environment. The unique cellular composition of the brain is largely different from other tissues, imposing a profound selective pressure on cancer cells and thus creating a spectrum of distinct molecular characteristics of the brain metastatic tumor cells. Consistent with previous reports, tumor cells exhibiting higher EMT status and mobility are more prone to use blood vessel co-option as the primary source of blood supply [34, 39, 40]. To date, the molecular traits of tumors that can predict vessel co-option are still lacking [26]. In this study, we established a molecular signature that can effectively distinguish tumors adopting blood vessel co-option and angiogenesis, validated by public datasets. Besides, we identified chemokine programs associated with the different blood supply strategies. For example, anti-angiogenic factors CXCL14 and CXCL9 were highly expressed in blood vessel co-option-related tumors [22]. Meanwhile, CXCL5, an angiogenesis promoter [29], was increased in angiogenesis-related tumors.

Although we systematically analyzed the transcriptomic landscape of GCBM, our study has some limitations. First, the paired primary gastric cancer tissues were not available for analysis. Second, due to the rarity of GCBM, we could not increase the sample size. Despite this, we included as many tissue areas as possible to reinforce the conclusions. In addition, data from external public databases have been used to validate the key observations from the study.

In summary, tumor cells, immune systems, and vascular systems constitute a highly interactive network in aggressive metastatic cancers. We illustrated the spatial molecular characteristics of immune response associated with specific vasculature approaches in GCBM. This would shed light upon the clinical combination of anti-vascular and immune therapies for aggressive metastatic cancers.

Supplementary Data

Supplementary data is available at *Gastroenterology Report* online.

Authors' Contributions

K.L. and D.Z. (Dongsheng Zhang) conceived and designed the project. K.L., C.W., C.G., and Y.Z. (Yu Zhong) collected and prepared the samples. Y.L. (Yunxin Lu), F.L., and Y.Z. (Yang Zhang) did patient management and selection. C.W. did the pathological examination. D.Z. (Dun Zhang) and Y.Z. (Yu Zhong) collected the clinical data. K.L. and Y.W. did the data curation and statistical analysis. L.Y. (Lin Yin) conducted the bioinformatical analysis. K.L. wrote the manuscript. D.Z. (Dongsheng Zhang) applied for funding and reviewed the manuscript. All the authors read and approved the final manuscript.

Conflicts of Interest

None declared.

References

1. Kotecha R, Gondi V, Ahluwalia MS *et al.* Recent advances in managing brain metastasis. *F1000Res* 2018;**7**:1772.
2. Nayak L, Lee EQ, Wen PY. Epidemiology of brain metastases. *Curr Oncol Rep* 2012;**14**:48–54.
3. Boire A, Brastianos PK, Garzia L *et al.* Brain metastasis. *Nat Rev Cancer* 2020;**20**:4–11.
4. Kasakura Y, Fujii M, Mochizuki F *et al.* Clinicopathological study of brain metastasis in gastric cancer patients. *Surg Today* 2000;**30**:485–90.
5. Go PH, Klaassen Z, Meadows MC *et al.* Gastrointestinal cancer and brain metastasis: a rare and ominous sign. *Cancer* 2011;**117**:3630–40.
6. Lee JL, Kang YK, Kim TW *et al.* Leptomeningeal carcinomatosis in gastric cancer. *J Neurooncol* 2004;**66**:167–74.
7. York JE, Stringer J, Ajani JA *et al.* Gastric cancer and metastasis to the brain. *Ann Surg Oncol* 1999;**6**:771–6.
8. Rao A, Barkley D, Franca GS *et al.* Exploring tissue architecture using spatial transcriptomics. *Nature* 2021;**596**:211–20.
9. Marx V. Method of the Year: spatially resolved transcriptomics. *Nat Methods* 2021;**18**:9–14.
10. Jerby-Arnon L, Neftel C, Shore ME *et al.* Opposing immune and genetic mechanisms shape oncogenic programs in synovial sarcoma. *Nat Med* 2021;**27**:289–300.
11. Yoosuf N, Navarro JF, Salmen F *et al.* Identification and transfer of spatial transcriptomics signatures for cancer diagnosis. *Breast Cancer Res* 2020;**22**:6.
12. Wu K, Lin K, Li X *et al.* Redefining tumor-associated macrophage subpopulations and functions in the tumor microenvironment. *Front Immunol* 2020;**11**:1731.
13. He B, Bergenstrahle L, Stenbeck L *et al.* Integrating spatial gene expression and breast tumour morphology via deep learning. *Nat Biomed Eng* 2020;**4**:827–34.
14. Schurch CM, Bhate SS, Barlow GL *et al.* Coordinated cellular neighborhoods orchestrate antitumoral immunity at the colorectal cancer invasive front. *Cell* 2020;**182**:1341–59.e19.
15. Zhao E, Stone MR, Ren X *et al.* Spatial transcriptomics at subspot resolution with BayesSpace. *Nat Biotechnol* 2021;**39**:1375–84.
16. Danaher P, Kim Y, Nelson B *et al.* Advances in mixed cell deconvolution enable quantification of cell types in spatial transcriptomic data. *Nat Commun* 2022;**13**:385.
17. Toki MI, Merritt CR, Wong PF *et al.* High-plex predictive marker discovery for melanoma immunotherapy-treated patients using digital spatial profiling. *Clin Cancer Res* 2019;**25**:5503–12.

18. Jin S, Li R, Chen MY *et al.* Single-cell transcriptomic analysis defines the interplay between tumor cells, viral infection, and the microenvironment in nasopharyngeal carcinoma. *Cell Res* 2020;**30**:950–65.

19. Dorner BG, Dorner MB, Zhou X *et al.* Selective expression of the chemokine receptor XCR1 on cross-presenting dendritic cells determines cooperation with CD8+ T cells. *Immunity* 2009;**31**:823–33.

20. Mu R, Zhang Z, Han C *et al.* Tumor-associated macrophages-educated reparative macrophages promote diabetic wound healing. *EMBO Mol Med* 2023;**15**:e16671.

21. Ma RY, Black A, Qian BZ. Macrophage diversity in cancer revisited in the era of single-cell omics. *Trends Immunol* 2022;**43**:546–63.

22. Bule P, Aguiar SI, Aires-Da-Silva F *et al.* Chemokine-directed tumor microenvironment modulation in cancer immunotherapy. *Int J Mol Sci* 2021;**22**(18):9804.

23. Lv H, Lv G, Chen C *et al.* NAD(+) metabolism maintains inducible PD-L1 expression to drive tumor immune evasion. *Cell Metab* 2021;**33**:110–27.e5.

24. Li M, Kirtane AR, Kiyokawa J *et al.* Local targeting of NAD(+) salvage pathway alters the immune tumor microenvironment and enhances checkpoint immunotherapy in glioblastoma. *Cancer Res* 2020;**80**:5024–34.

25. Muller H, Schmiedl A, Weiss C *et al.* DMBT1 is upregulated in lung epithelial cells after hypoxia and changes surfactant ultrastructure. *Pediatr Pulmonol* 2020;**55**:2964–9.

26. Kuczynski EA, Vermeulen PB, Pezzella F *et al.* Vessel co-option in cancer. *Nat Rev Clin Oncol* 2019;**16**:469–93.

27. Kumar S, Liu J, Pang P *et al.* Sox9 activation highlights a cellular pathway of renal repair in the acutely injured mammalian kidney. *Cell Rep* 2015;**12**:1325–38.

28. Zhao S, Huang Z, Jiang H *et al.* Sirtuin 1 induces choroidal neovascularization and triggers age-related macular degeneration by promoting LCN2 through SOX9 Deacetylation. *Oxid Med Cell Longev* 2022;**2022**:1671438.

29. Kjolle S, Finne K, Birkeland E *et al.* Hypoxia induced responses are reflected in the stromal proteome of breast cancer. *Nat Commun* 2023;**14**:3724.

30. Palmieri V, Lazaris A, Mayer TZ *et al.* Neutrophils expressing lysyl oxidase-like 4 protein are present in colorectal cancer liver metastases resistant to anti-angiogenic therapy. *J Pathol* 2020;**251**:213–23.

31. Donnem T, Hu J, Ferguson M *et al.* Vessel co-option in primary human tumors and metastases: an obstacle to effective anti-angiogenic treatment? *Cancer Med* 2013;**2**:427–36.

32. Frentzas S, Simoneau E, Bridgeman VL *et al.* Vessel co-option mediates resistance to anti-angiogenic therapy in liver metastases. *Nat Med* 2016;**22**:1294–302.

33. Leenders WP, Kusters B, Verrijp K *et al.* Antiangiogenic therapy of cerebral melanoma metastases results in sustained tumor progression via vessel co-option. *Clin Cancer Res* 2004;**10**:6222–30.

34. Kuczynski EA, Yin M, Bar-Zion A *et al.* Co-option of liver vessels and not sprouting angiogenesis drives acquired sorafenib resistance in hepatocellular carcinoma. *J Natl Cancer Inst* 2016;**108**(8):djw030.

35. Makker V, Rasco D, Vogelzang NJ *et al.* Lenvatinib plus pembrolizumab in patients with advanced endometrial cancer: an interim analysis of a multicentre, open-label, single-arm, phase 2 trial. *Lancet Oncol* 2019;**20**:711–8.

36. Kawazoe A, Fukuoka S, Nakamura Y *et al.* Lenvatinib plus pembrolizumab in patients with advanced gastric cancer in the first-line or second-line setting (EPOC1706): an open-label, single-arm, phase 2 trial. *Lancet Oncol* 2020;**21**:1057–65.

37. Taylor MH, Lee CH, Makker V *et al.* Phase IB/II trial of lenvatinib plus pembrolizumab in patients with advanced renal cell carcinoma, endometrial cancer, and other selected advanced solid tumors. *J Clin Oncol* 2020;**38**:1154–63.

38. Cheng S, Li Z, Gao R *et al.* A pan-cancer single-cell transcriptional atlas of tumor infiltrating myeloid cells. *Cell* 2021;**184**:792–809.e23.

39. Kienast Y, von Baumgarten L, Fuhrmann M *et al.* Real-time imaging reveals the single steps of brain metastasis formation. *Nat Med* 2010;**16**:116–22.

40. Depner C, Zum Buttel H, Bogurcu N *et al.* EphrinB2 repression through ZEB2 mediates tumour invasion and anti-angiogenic resistance. *Nat Commun* 2016;**7**:12329.